


# Transport and spectral properties of magic-angle twisted bilayer graphene junctions based on local orbital models

M. Alvarado and A. Levy Yeyati *Departamento de Física Teórica de la Materia Condensada C-V, Condensed Matter Physics Center (IFIMAC) and Instituto Nicolás Cabrera, Universidad Autónoma de Madrid, E-28049 Madrid, Spain*

(Received 21 May 2021; revised 19 July 2021; accepted 26 July 2021; published 4 August 2021)

The electronic properties of junctions defined electrostatically on twisted bilayer graphene can be addressed theoretically using lattice models. Recent works have introduced minimal local orbital models to describe twisted bilayer graphene at the magic angle (MATBLG) with different degrees of approximation and accounting for fragile topology. Based on these models and using Green's function techniques we analyze in this work the spectral and transport properties for MATBLG defined along different types of edges. To this end we first study the effect of symmetry breaking perturbations on the bulk bands, identifying their topological character. In a second step we obtain results for the local spectral densities at open boundaries and for two terminal transport on a three region junction where one could control independently the central and lateral regions doping level. Due to the large moiré length we observe that the hybridization of chiral edge states on these junctions gives rise to a signature in the longitudinal transport and to asymmetries in the local densities of states. We further show that these properties are extremely sensitive to the orientation of the junctions along the moiré lattice.

DOI: [10.1103/PhysRevB.104.075406](https://doi.org/10.1103/PhysRevB.104.075406)

## I. INTRODUCTION

The ability to tune the electronic properties of van der Waals heterostructures of two-dimensional materials by changing their relative angle has given rise to the new field of “twistronics” [1,2]. Twisted bilayer graphene is by now the most prominent example of this field, exhibiting a large variety of interesting phenomena. Near the so-called magic angle the flat bands close to the charge neutrality point (CNP) arising from the large scale moiré pattern become extremely sensitive to electronic correlations and interactions, giving rise to a rich phase diagram including superconducting and insulating phases as a function of the doping level [3,4]. The flat bands also exhibit topological properties [5] which manifest for example in the appearance of anomalous quantum Hall effect [6–8]. More recently, the possibility to produce tunable junctions on this material by local electrostatic control has been demonstrated [9], thus opening the way towards its application in transport devices.

From the point of view of theory, large efforts have been devoted to understanding the origin of correlation induced phenomena in magic-angle twisted bilayer graphene [10–19]. A basic debate has emerged regarding the appropriate microscopic modeling. While the continuous model of Bistritzer and MacDonald [20] is broadly accepted as an accurate starting single-particle description, real space or lattice models could be more appropriate for the inclusion of interactions or for the study of transport in MATBLG junctions. Lattice models suffer, however, from the so-called Wannier obstruction [21–26], which prevents the description of topological bands in terms of local orbitals. While simple low energy two bands models were proposed which avoid this problem

by neglecting certain symmetries [27], so called “faithful” tight-binding (TB) models including higher energy bands are able to account properly for the fragile topology [28–34] of the low energy bands [24,35]. Other models have been proposed mixing real and momentum space descriptions [36], or including both valleys in a two-band description [37].

Our starting point is the lattice models from Refs. [27,35] for which we construct the boundary Green's functions (bGFs) using an efficient method [38] for different type of edges. Furthermore it is known that the one-electron bands in MATBLG are greatly distorted near the magic angle by the effect of either electron-electron interactions and by the interaction with the substrate [11–14,39,40]. To simulate their effect we introduce in the models symmetry breaking terms describing the coupling to the hBN substrate and possible charge density wave (CDW) modulations. This allows us to study the effect of most characteristic nonmagnetic perturbations in MATBLG.

Interactions also lead to phases with broken valley and spin symmetries which manifest in the so-called cascade transitions as a function of the doping level [7,41]. In this work we do not aim to make predictions on the system phase diagram. We rather assume that valley and spin degrees of freedom can be independently populated and study the resulting spectral and transport properties for a given configuration.

An important aspect of MATBLG which guides our study is that the large size of its moiré pattern ( $>10$  nm) would allow transport experiments on junctions along well defined directions on the moiré lattice. As we show in this work, the junction's orientation plays an important role on its transport and spectral properties giving rise to specific signatures in

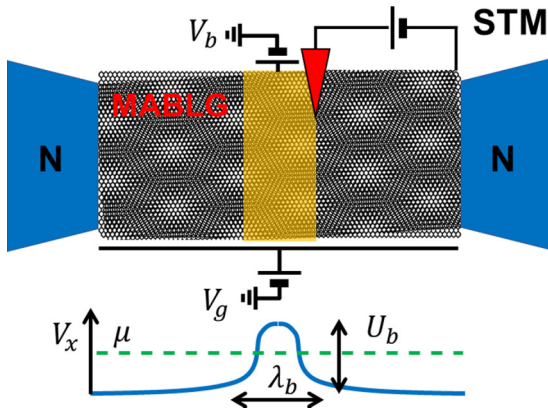


FIG. 1. Experimental setup based on MATBLG analyzed in this work. We show two terminal transport through a barrier defined by a backgate. The length of the barrier region can vary between  $\lambda_b \approx 100$  and  $300$  nm. The large size of the moiré pattern would allow one to study the effect of the alignment of the junction along well defined directions on the moiré lattice using transport measurements and STM techniques.

the longitudinal transport and density of states asymmetries along the junction. Inspired by the recent experiments of Ref. [9] we study transport through nonhomogeneous regions with varying doping levels which could be tuned by gates as schematically shown in Fig. 1. Additionally, our approach should allow us to predict the local spectral properties at such junctions or at the edges of TBLG samples, which could be accessed experimentally as demonstrated in recent STM studies on NbSe<sub>2</sub>/CrBr<sub>3</sub> moiré superlattices [42].

The rest of the manuscript is organized as follows: in Sec. II, we discuss the effect of Wannier obstruction and fragile topology of the nearly flat bands of MATBLG in lattice models. We introduce the models from Refs. [27,35] and their relevant symmetries and topology. We implement different nonmagnetic symmetry breaking perturbations that can open topological gaps at the Fermi energy. Furthermore, using Wilson loops we obtain the band's Chern number and study the competition among these perturbations in determining the band's topology.

In Sec. III, we study the spectral properties at edges of MATBLG starting with a zig-zag boundary exhibiting edge states at the CNP and at the moiré gap between the nearly flat bands and the excited ones. Moreover, we show the appearance of chiral edge states at the CNP due to sublattice symmetry breaking perturbation in the model of Ref. [35] unlike the gapped spectrum for the perturbed model of Ref. [27]. In Sec. IV, we study spectral and transport properties in a three region device where we can modulate the doping levels, analyzing the influence of topological states at the boundaries of the central region and the orientation of those boundaries.

We finally offer, in Sec. V, some conclusions summarizing the main results and give an outlook of possible future work taking advantage of the methods developed here. Technical details like the explicit description of the tight-binding models, some notes on the boundary Green's functions for these lattice models [43], or the recursive GF method to obtain the

transport properties in inhomogeneous devices are included in three Appendices.

## II. LATTICE MODELS FOR MATBLG

Close to the magic angle a lattice model based on the  $\pi$  orbitals at the carbon atoms requires more than 10 000 states for each moiré unit cell. The idea of minimal lattice models for MATBLG is to construct a basis of well-localized Wannier orbitals purely consisting of flat band states. While this idea is extremely attractive, simple two-bands lattice models fail to describe the nontrivial topology of the flat bands, which is linked to the fact that they arise from two unperturbed Dirac cones coming from different graphene layers but the same graphene valley, thus carrying the same helicity. The topological character of the bands obstructs the construction of minimal two-bands models based on Wannier orbitals with the correct topology, although they can reproduce the bands dispersion [27]. Adding higher energy trivial bands is necessary to consider all the emergent symmetries of the problem in the hypothesis of fragile topology [35]. In spite of these limitations we found it instructive to study first the case of the simplest two band model of Ref. [27] and then to extend our study to the six band model of Ref. [35] that accounts for fragile topology. We shall refer to these two models as two-band-one-valley (2B1V) and six-band-one-valley (6B1V) models, respectively.

### A. 2B1V model

Due to the fact that the flat bands are isolated from the rest of the high energy bands, this two-band minimal model pursues to capture the electronic properties of these bands in a basis of well-localized Wannier orbitals. The Wannier orbitals in the flat bands are placed around the  $A = A_1B_2$  and  $B = B_1A_2$  sites [see Fig. 2(a)] in the emergent honeycomb moiré lattice, where the subindex refers to different pristine graphene layers in TBG. This description reproduces the observed centering of charge around AA sites in the moiré lattice. From the localized Wannier description a tight binding Hamiltonian is derived by calculating the hopping integrals between these well localized Wannier orbitals, which behave as  $(p_x, p_y)$  orbitals residing each one in one site of the honeycomb lattice. To describe quantitatively the TBG band dispersion it is necessary to take into account hopping elements between an increasing number of neighbors due to the rather extended character of the Wannier orbitals representing the flat bands. This model has been intensively used [44–47] due to its simplicity but, although it exhibits naturally particle/hole symmetry, due to the Wannier obstruction it lacks the characteristic symmetries of the system [35] and leads to moiré minivalleys with vanishing net chirality.

Following Ref. [44] we truncate the hopping terms in the 2B1V model by considering just the four largest ones. As we can see in Table I, due to the particular form of the Wannier orbitals the hopping elements do not vary monotonically with distance (i.e., for instance,  $t_5 > t_4$ ). The relative size of the hopping elements considered is illustrated in Fig. 2(a). Within this approximation the bulk Hamiltonian within the 2B1V

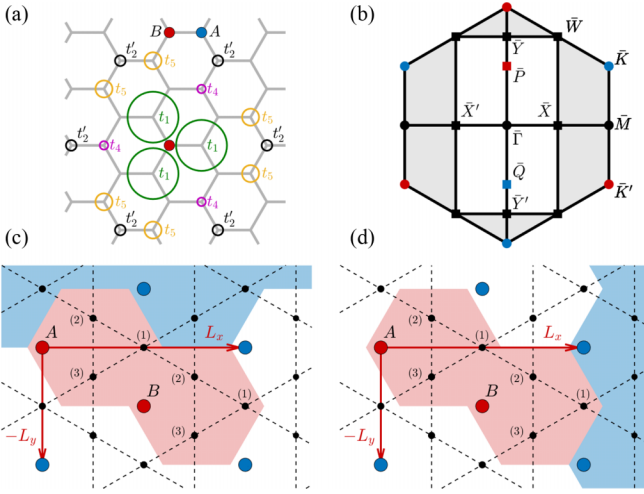


FIG. 2. Real space representation and corresponding BZs for the 2B1V and 6B1V models. Panel (a) shows the honeycomb lattice and the nonmonotonic variation with distance of the hopping integrals ( $t_1, t_2, t_4, t_5$ ) from a lattice site  $B$  for the 2B1V model. (b) Triangular (gray shaded) and rectangular (white) moiré BZ showing the high symmetry points in each one. The overline in the high symmetry points indicates that they belong to the moiré BZ. Lower panels correspond to the 6B1V model indicating the armchair (c) and zigzag (d) boundaries in real space. The  $p$  orbitals are centered at the unit cell site red dots ( $A, B$ ) forming a triangular lattice and the black dots correspond to the  $s$  orbitals placed in a kagome lattice with three sites per unit cell. The shaded red region in (c) and (d) corresponds to the doubling of the triangular primitive cell with orthogonal lattice vectors producing the folding of the original triangular BZ into a rectangular one as indicated in panel (b).

model is given by

$$\hat{\mathcal{H}}_{\pm}^{(2)}(\mathbf{k}) = \begin{pmatrix} \pm t_2' g(\mathbf{k}) & h(\mathbf{k}) \\ h(\mathbf{k})^* & \pm t_2' g(\mathbf{k}) \end{pmatrix},$$

$$h(\mathbf{k}) = t_1 f_1(\mathbf{k}) + t_4 f_4(\mathbf{k}) + t_5 f_5(\mathbf{k}), \quad (1)$$

where the subindex  $\xi = \pm$  indicates the valley,  $t_2 \approx it_2'$ , and

$$g(\mathbf{k}) = 2 \sin[\mathbf{k}(2\mathbf{L}_2 - \mathbf{L}_1)] + 2 \sin[\mathbf{k}(2\mathbf{L}_1 - \mathbf{L}_2)] - 2 \sin[\mathbf{k}(\mathbf{L}_1 + \mathbf{L}_2)],$$

$$f_1(\mathbf{k}) = 1 + e^{i\mathbf{k}\mathbf{L}_1} + e^{i\mathbf{k}\mathbf{L}_2},$$

$$f_4(\mathbf{k}) = e^{i\mathbf{k}(\mathbf{L}_1 + \mathbf{L}_2)} + 2 \cos[\mathbf{k}(\mathbf{L}_1 - \mathbf{L}_2)],$$

$$f_5(\mathbf{k}) = e^{i2\mathbf{k}\mathbf{L}_1} + e^{i2\mathbf{k}\mathbf{L}_2} + e^{-i\mathbf{k}\mathbf{L}_1} + e^{-i\mathbf{k}\mathbf{L}_2} + e^{i\mathbf{k}(2\mathbf{L}_1 - \mathbf{L}_2)} + e^{i\mathbf{k}(2\mathbf{L}_2 - \mathbf{L}_1)}, \quad (2)$$

TABLE I. Hopping amplitudes for the 2B1V model of Ref. [27] written in units of the dominant energy scale  $t_1 = 1.2$  meV assuming  $t_2 \approx it_2'$ .

Parameter	Meaning	Ratio to $t_1$
$t_1$	( $A - B$ ) first-NN hopping	1
$t_2'$	( $A - A$ ) second-NN hopping	0.208
$t_4$	( $A - B$ ) second-NN hopping	0.167
$t_5$	( $A - B$ ) third-NN hopping	0.333

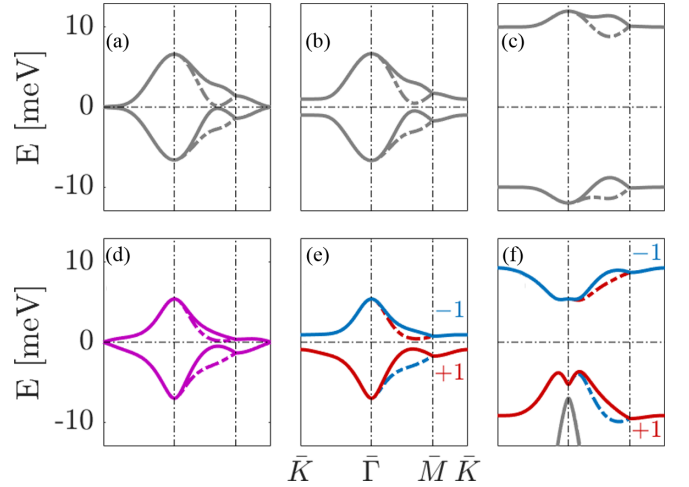


FIG. 3. Evolution of the nearly flat bands in the hexagonal BZ for the 2B1V (upper panels) and 6B1V (lower panels) models due to the sublattice symmetry breaking parameter  $\delta_S$ , which takes the values 0, 1, and 10 meV for each column, respectively. Color code: gray bands indicate trivial topological character while colored ones have topological nature. Straight and dashed-dotted lines correspond to different global valleys. Red (blue) is associated to bands with Chern number +1 (−1); on the other hand, magenta means fragile topology bands as in panel (d).

where the lattice vectors are  $\mathbf{L}_{1,2} = L_m(\sqrt{3}/2, \pm 1/2)$  and  $L_m = a/(2 \sin \theta/2)$  is the moiré lattice vector (given in terms of the graphene lattice parameter  $a$  and the twist angle  $\theta$ ). The list of the parameters used is given in Table I.

A gap may be opened by breaking the sublattice symmetry which protects the Dirac nodes with a perturbation of the form  $\hat{\mathcal{H}}_{\pm}'(\mathbf{k}) = \hat{\mathcal{H}}(\mathbf{k})_{\pm} + \delta_S \sigma_z$ . This could be associated either to the effect of the substrate or arising from interactions treated perturbatively in a mean field approximation. In this work we shall consider  $\delta_S$  as a phenomenological parameter.

The flat bands in the triangular moiré Brillouin zone (BZ) for the 2B1V model are shown in the upper upper panels of Fig. 3. Full and dashed lines correspond to the two graphene valleys and panels (a), (b), and (c) illustrate the effect of the  $\delta_S$  parameter opening a gap at the Dirac nodes, which in this model have opposite helicity and thus are trivial in nature.

### B. 6B1V model

Reference [35] discusses how to build “faithful” TB models avoiding the topological obstruction by adding different sets of trivial bands to the flat ones. These models should satisfy the requirements imposed by the relevant symmetries of the system plus the nontrivial topology of the flat bands; and also that the complementary set of trivial bands describe quantitatively the higher energy bands in MATBLG. For that purpose Ref. [35] obtains an atomic limit for the sum of the topological flat bands plus the determined set of trivial bands with the constraints of having two isolated bands with the appropriate momentum-space symmetry representations. This results in a basis of  $p_z$  and  $p_{\pm}$  orbitals in a triangular lattice ( $\tau, p_z$ ) and ( $\tau, p_{\pm}$ ), respectively, and three  $s$  orbitals in a kagome lattice ( $\kappa, s$ ), using a notation that indicates the

lattice (triangular,  $\tau$ , or kagome,  $\kappa$ ) and the character of the orbitals ( $s$  or  $p$ ). The two ( $\tau$ ,  $p_{\pm}$ ) orbitals sitting on a triangular lattice are based on the charge centers in MATBLG at the flat bands placed at the A-A bonds in a triangular moiré lattice giving rise to the Dirac nodes of the flat bands; see Figs. 2(c) and 2(d).

Details on the 6B1V model as defined on a minimal triangular unit cell can be found in Ref. [35]. Here we extend it to situations where there could be cell doubling (cd) due to interactions producing charge transfer between neighboring sites [10,14,15,39,47]. This unit-cell doubling leads to an orthogonal lattice with vectors  $L_x = \sqrt{3}L_m$  and  $L_y = L_m$ , where we can define two different types of edges: armchair (AC) and zig-zag (ZZ), in resemblance of pristine graphene; see lower panels of Fig. 2. The local fermion operators are defined as  $\hat{\Psi} = (\hat{\Psi}_A \ \hat{\Psi}_B)^T$ , with  $\hat{\Psi}_{\mu} = (\hat{\tau}_{p_z, \mu} \ \hat{\tau}_{p_+, \mu} \ \hat{\tau}_{p_-, \mu} \ \hat{\kappa}_{s, \mu}^{(1)} \ \hat{\kappa}_{s, \mu}^{(2)} \ \hat{\kappa}_{s, \mu}^{(3)})^T$ , where  $\mu \equiv A, B$  indicates the two sites within the orthogonal cell. Within this basis the 6B1V Hamiltonian adopts the form

$$\hat{\mathcal{H}}_{cd}^{(6)}(\mathbf{k}) = \begin{pmatrix} \hat{H}^{AA} & \hat{H}^{AB} \\ \hat{H}^{AB\dagger} & \hat{H}^{AA} \end{pmatrix}, \quad (3)$$

where

$$\hat{H}^{AA} = \begin{pmatrix} H_{p_z}^{AA} + \mu_{p_z} & \hat{C}_{p_{\pm}p_z}^{AA} & \hat{0} \\ \hat{C}_{p_{\pm}p_z}^{AA\dagger} & \hat{H}_{p_{\pm}}^{AA} + \mu_{p_{\pm}} \hat{\mathbb{I}}_2 & \hat{C}_{\kappa p_{\pm}}^{AA} \\ \hat{0} & \hat{C}_{\kappa p_{\pm}}^{AA\dagger} & \hat{H}_{\kappa}^{AA} + \mu_{\kappa} \hat{\mathbb{I}}_3 \end{pmatrix},$$

$$\hat{H}^{AB} = \begin{pmatrix} H_{p_z}^{AB} & \hat{C}_{p_{\pm}p_z,1}^{AB} & \hat{0} \\ \hat{C}_{p_{\pm}p_z,2}^{AB} & \hat{H}_{p_{\pm}}^{AB} & \hat{C}_{\kappa p_{\pm},1}^{AB} \\ \hat{0} & \hat{C}_{\kappa p_{\pm},2}^{AB} & \hat{H}_{\kappa}^{AB} \end{pmatrix}. \quad (4)$$

The expressions for the matrices  $H_{\alpha}^{\mu\nu}$  and  $C_{\alpha\beta}^{\mu\nu}$  are given in Appendix A. The diagonal elements are set by  $\mu_{p_z} \equiv -6t_{p_z} + \delta_{p_z}$ ,  $\mu_{p_{\pm}} \equiv 3t_{p_{\pm}} + \delta_{p_{\pm}}$ , and  $\mu_{\kappa} \equiv -4(t_{\kappa} + t'_{\kappa}) + \delta_{\kappa}$ .

In addition, we will consider the following symmetry breaking perturbations:

$$\hat{H}_{cd}^S = \delta_S \tau_z^{p_{\pm}} \sigma_0, \quad \hat{H}_{cd}^{CDW} = \delta_{CDW} \hat{\mathbb{I}}_6 \sigma_z, \quad (5)$$

where  $\tau_z^{p_{\pm}}$  is a Pauli matrix acting in the  $(\tau, p_{\pm})_{\mu}$  orbitals with  $\mu = (A, B)$ ,  $\sigma_0$  is the identity matrix, and  $\sigma_{\mu}$  are Pauli matrices which act in the  $(A - B)$  doubled unit cell sites' space. The  $\delta_S$  parameter is equivalent to a sublattice staggered moiré potential as pointed out in Ref. [19].

The total Hamiltonian in the 6B1V model is then given by

$$\hat{\mathcal{H}}_{cd}^{(6)'}(\mathbf{k}) = \hat{\mathcal{H}}_{cd}^{(6)}(\mathbf{k}) + \hat{H}_{cd}^S + \hat{H}_{cd}^{CDW}. \quad (6)$$

These perturbations can be either associated to the effect of the substrate (i.e., hBN substrate induces sublattice symmetry breaking in the graphene lattice placed on top) or to a CDW arising from interactions (i.e., breaking translational symmetry) allowing us to explore a larger phase space [11–15,39,47].

On the lower panels of Fig. 3 we show the flat bands in the triangular BZ for the 6B1V model for increasing values of the gap opening parameter  $\delta_S$ . As can be observed, for  $\delta_S = 0$  the bands within the 2B1V and the 6B1V models are quite similar despite the absent electron/hole symmetry in the 6B1V model. For sufficiently large  $\delta_S$  their behavior differs substantially. While in the 2B1V model the band minimum

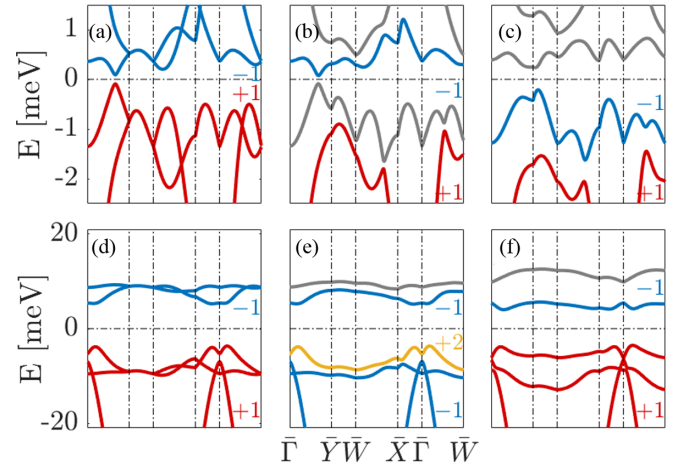


FIG. 4. Evolution of the nearly flat bands in the rectangular BZ for one valley in the 6B1V model due to the translational symmetry breaking potential. Upper panels show low coupling limit with the substrate  $\delta_S = 0.1$  meV and  $\delta_{CDW} = 0, 0.3$ , and 1 meV for each panel (a), (b), and (c), respectively. From panel (b) to (c) we observe a topological phase transition. Lower panels show the strong coupling limit to the substrate  $\delta_S = 10$  meV and translational symmetry breaking potential  $\delta_{CDW} = 0, 1$ , and 4 meV. Color code: gray bands indicates trivial topological character, while colored ones have topological nature. Red (blue) is associated to bands with Chern number +1 (−1); yellow in panel (e) corresponds to Chern number +2.

continues to appear at  $\bar{K}$  and  $\bar{K}'$ , for the 6B1V model the minimum is transferred into the  $\bar{\Gamma}$  point. This behavior (which was also pointed out in Refs. [10,39]) is due to the fact that the states at the  $\bar{\Gamma}$  point in the 6B1V model are a combination of the  $(\tau, p_z)$  and  $(\kappa, s)$  orbitals, which are coupled to the perturbed  $(\tau, p_{\pm})$  ones.

The models differ, as expected, on their topological properties. The different colors in Fig. 3 indicate the bands' Chern number as extracted from the winding of the Berry curvature in the BZ of the corresponding Wilson loops [48–51]. When  $\delta_S \neq 0$  the positive and negative energy flat bands at the CNP in the 6B1V model are characterized by a nonzero Chern number. A change in the global valley induces a change in sign of the Chern number for each band due to time reversal symmetry. The 2B1V bands remain trivial in all cases.

The effect of the translation symmetry breaking parameter  $\delta_{CDW}$  and the combined effect of  $\delta_{CDW}$  and  $\delta_S$  in the 6B1V model are illustrated in Fig. 4. In the upper panels of Fig. 4 we show the low energy bands in the orthogonal BZ for weak coupling with the substrate ( $\delta_S = 0.1$  meV) and varying  $\delta_{CDW}$ . The former opens a gap at the CNP and the latter splits each nearly flat band as shown in panel (b), redistributing the topological charge of the original flat bands in a set of splitted trivial and topological bands. The total topological charge at charge neutrality is still  $C = +1$ . By effect of the competing perturbations a gap closing occurs due to a band inversion that produces in panel (c) the trivialization at the CNP.

On the other hand, in the lower panels of Fig. 4 we show the effect of translational symmetry breaking in the case of strong coupling with the substrate ( $\delta_S = 10$  meV). As before  $\delta_{CDW}$  splits the flat bands and redistributes the topological charge between the new set of bands. In this case the lower flat bands



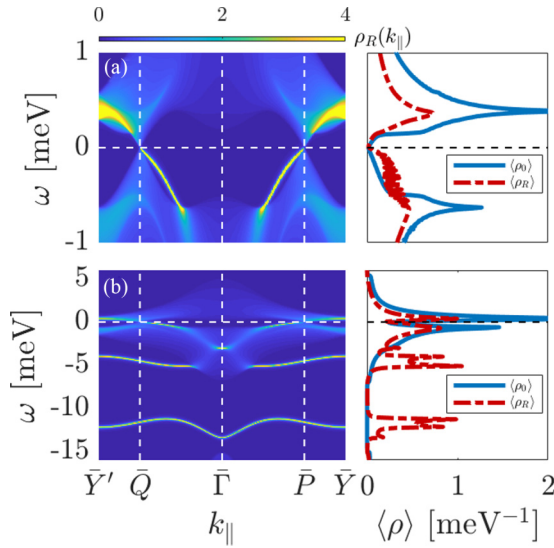


FIG. 5. Open ZZ boundary LDOS for the 6B1V model without symmetry breaking perturbations. The left column corresponds to the spectral density for a right boundary, while the right column shows the integrated LDOS where the straight (dot-dashed) line represents bulk LDOS  $\langle\rho_0\rangle$  (right boundary LDOS  $\langle\rho_R\rangle$ ). The upper and lower panels show the same results but in different energy scale. In panel (a) we can observe trivial edge states inherit from pristine monolayer graphene appearing within the nearly flat bands. Panel (b) illustrates the appearance of moiré edge states in the gap between nearly flat and the lower energy bands.

are crossed by the set of trivial occupied bands. Although the Chern number at charge neutrality in panel (e) is  $C = +1$ , the redistribution of topological charge is completely different due to the effect of the excited bands which, individually considered, can carry some topological order. For this reason we observe a flat band with  $C = +2$ . In the subsequent panels we observe different topological transitions: first in panel (f) a gap closing between the lower topological bands that sets  $C = +1$  to the flat band close to the charge neutrality and trivializes the rest of the lowest bands and finally if we further increase  $\delta_{\text{CDW}}$  a band inversion occurs between the flat bands close to the CNP (not included).

The competition between Chern insulating states and CDW in TBLG has been recently analyzed in Refs. [12,13,18]. As we can see in Fig. 4, starting from a Chern insulating phase the breaking of translational symmetry can lead to a trivial phase, in agreement with these works.

### III. SPECTRAL PROPERTIES AT EDGES

The bGF  $\hat{G}_{L,R}$  of the semi-infinite system obtained as described in Appendix B allows us to analyze the spectral properties at the edges of MATBLG, encoded in the spectral densities  $\rho_{L,R}(k_{||}, \omega) = \text{Im}\hat{G}_{L,R}(k_{||}, \omega)/\pi$  and the LDOS  $\langle\rho_{L,R}(\omega)\rangle = \int dk_{||}/\Omega_{k_{||}} \rho_{L,R}(k_{||}, \omega)$ , where  $\Omega_{k_{||}} = 2\pi/L_{||}$  accounts for the limits of integration.

The edge spectral properties are radically different in the 6B1V model to the 2B1V where only trivial states can be observed. Due to the contribution of the set of higher energy bands in the 6B1V model we can distinguish two types of edge states in Fig. 5: the ones inherited from the pristine graphene

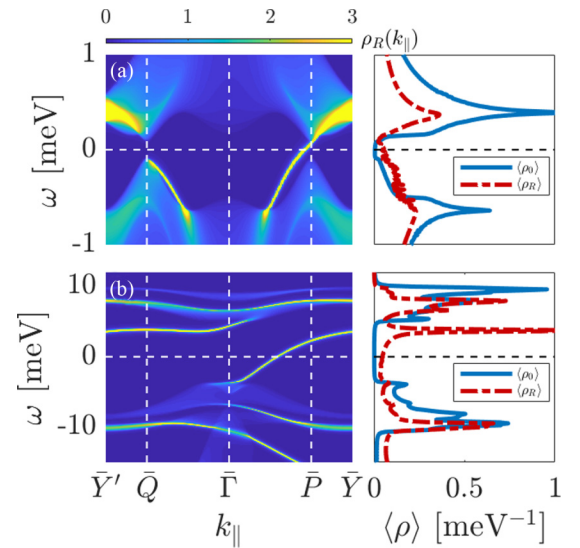


FIG. 6. Same as Fig. 5 but under the effect of the coupling with the substrate  $\delta_S$  and broken translation symmetry  $\delta_{\text{CDW}}$ . Panel (a): weak coupling with the substrate ( $\delta_S = 0.1$  meV) where interactions open a gap without distorting the bands. It shows the appearance of a topological edge state between the flat bands at the  $\bar{P}$  minivalley. Panel (b): strong coupling with the substrate ( $\delta_S = 10$  meV) where interactions distort the bands and the breaking of translational symmetry with  $\delta_{\text{CDW}} = 1$  meV splits both flat bands. One can observe topological edge states between the flat bands and another topological state with opposite chirality between the splitted flat band and the lower energy bands due to breaking of translation symmetry.

appearing at the CNP at each minivalley ( $\bar{Q}$  and  $\bar{P}$ ) in panel (a) and the ones that emerge entirely from the moiré structure at the gap between the flat bands and the excited ones [45] [see panel (b)]. One of these moiré edge states merges with the flat bands at  $\bar{\Gamma}$  and the other one is gapped and nearly dispersionless. This gapped edge state also appears at the AC boundary and might be related to higher order topology [52–54].

A gap opening at the CNP allows us to confirm the topological character of the nearly flat bands. In Fig. 6(a) for a right ZZ boundary a trivial edge state persists around the  $\bar{Q}$  minivalley (similar to the 2B1V case) and there appears a chiral edge state around  $\bar{P}$  minivalley in the weak coupling limit with  $\delta_S = 0.1$  meV. In addition, the left boundary shows a topological edge state with opposite chirality at  $\bar{Q}$ .

In panel (b) we can analyze the effect of  $\delta_{\text{CDW}}$  in the strong coupling limit,  $\delta_S = 10$  meV. In the first place, there appears a chiral edge state at charge neutrality between the new band minima around  $\bar{\Gamma}$  and thus it loses the minivalley character which was present in panel (a). As we pointed out in Fig. 4(e), at CNP the occupied bands have  $C = +1$ . On the other side, the gap between the lower flat band and the rest of the lower energy bands has  $C = -1$ . For that reason we can observe another chiral edge state with opposite chirality with respect to the one at charge neutrality. Notice that changing the global valley degree of freedom we obtain a similar picture for each boundary where the topological edge states have the opposite chirality and appear at the opposite minivalley (results not shown).

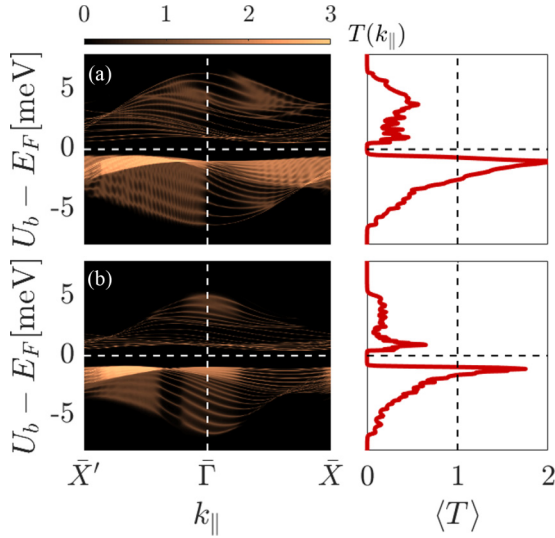


FIG. 7. Two-terminal transport for a three region junction device with AC orientation as a function of the height of the potential barrier  $U_b$  in the central region for (a) 2B1V and (b) 6B1V models. In both models we take  $\delta_S = 1$  meV. Left column: momentum resolved transmission of the junction. Right column: solid red line represents the average transmission. The length of the central region is  $\lambda_b \approx 160$  nm ( $\lambda_b^{\text{AC}} = 12L_y$ ) and the Fermi energy is kept at  $E_F = -1$  meV on the lateral regions.

#### IV. TRANSPORT AT N-N'-N JUNCTIONS

In this section we analyze two terminal transport in different types of MATBLG junctions. In Appendix C we use recursive GF techniques to take into account a nonuniform po-

tential profile in the central region, as in the situation depicted in Fig. 1.

The two-terminal conductance properties which are predicted by the 2B1V and 6B1V models in the situation of Fig. 1 are illustrated in Fig. 7 as a function of the height of the barrier,  $U_b$ , which defines the doping level in the central region. The lateral regions are kept at  $E_F = -1$  meV. For both models we include a finite gap opening parameter of the same size ( $\delta_S = 1$  meV). As can be observed, in Fig. 7 there is a qualitative and quantitative agreement between the two models, which reflects the fact that the topological character of the bands in the 6B1V model does not play a role in this case. In agreement with results of Ref. [44] for an abrupt barrier the momentum resolved transmission exhibits oscillations due to finite size effects. These spectral density oscillations are linked to the finite length of the central region  $\lambda_B$ . We can also observe that the normalized total transmission exhibits a maximum at the Van Hove singularity. A lower transmission is obtained when the barrier induces injection of states through the valence band.

The topological properties, however, do play a role in the case of N-N'-N junctions, where N' is kept at the CNP and the side regions are heavily doped. The outer regions in this junction exhibit smaller DOS than the flat bands, differing from the metallic behavior of heavily doped pristine graphene. The spectral properties for this type of junction are illustrated in Fig. 8. We consider two different orientations of the junctions with respect to the moiré lattice: AC [panels (a)–(d)] and ZZ [panels (e)–(h)]. As illustrated by these results, the orientation of the junctions leads to substantial differences even when the gate potential profile is kept constant.

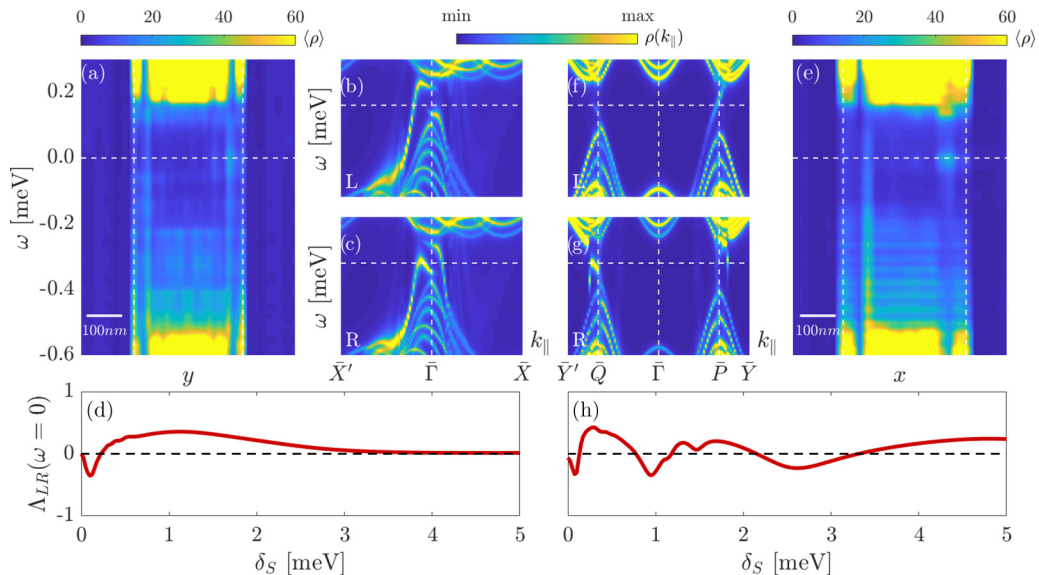


FIG. 8. Finite size effects in the local spectroscopy for a three region junction N-CNP-N with  $\delta_S = 0.1$  meV for both AC (left panels) and ZZ (right panels) boundaries. Panels (a) and (e): LDOS across the central region of the junction for AC and ZZ boundaries, respectively. We can observe anticrossings at low energies due to the hybridization of the edge states located at the ends of the central region. The central panels show the spectral density at both ends of the central region of each junction; upper (lower) ones show the left (right) end in arbitrary units. Panels (d) and (h) show the LDOS asymmetry dimensionless factor  $\Lambda_{LR}$  between the region ends at the CNP as a function of the sublattice symmetry breaking potential  $\delta_S$ . The length of the central region is  $\lambda_b \approx 270$  nm ( $\lambda_b^{\text{AC}} = 20L_y$  and  $\lambda_b^{\text{ZZ}} = 12L_x$ ) and its doping level is kept at the CNP; the lateral N regions are heavily doped with  $E_F = -140$  meV.

In the case of the armchair orientation we observe unexpected but mild left-right (LR) asymmetry in the LDOS. This is due to the sublattice symmetry breaking by  $\delta_S$ , which acts in the directional ( $\tau$ ,  $p_{\pm}$ ) orbitals. Due to the large penetration depth of the chiral edge states located at the ends of the central region we observe minigaps associated to hybridization of these states. The spectral densities of the boundaries show the hybridized opposite chirality end states. To analyze the evolution of the LR asymmetry as a function of  $\delta_S$  we define

$$\Lambda_{LR}(\omega) = \frac{\langle \rho_L(\omega) \rangle - \langle \rho_R(\omega) \rangle}{\langle \rho_L(\omega) \rangle + \langle \rho_R(\omega) \rangle}, \quad (7)$$

which corresponds to a LDOS LR asymmetry dimensionless factor. Panel (d) shows that in the limit  $\delta_S \rightarrow 0$  the AC junction does not show any LR asymmetry because without perturbations both AC boundaries are equivalent. Valley symmetry does not lift this LDOS asymmetry and only induces an inversion of the spectral density in  $k_{\parallel}$  (i.e., changing the chirality and minivalley of the topological edge states). The steplike increase of the LDOS at  $\omega \approx -0.15$  meV is due to the top of the valence band. The bottom of the conduction band is placed at  $\omega \approx 0.2$  meV.

On the other hand, ZZ junctions exhibit a much stronger LR asymmetry which survives even in the limit  $\delta_S \rightarrow 0$ ; see panel (h). Within the 6B1V model this is due to the definition of the unit cell and the effect of kagome orbitals at the boundaries, as can be seen in Fig. 2(d). Left (right) boundaries are defined on triangular (kagome) sites and for that reason both boundaries are naturally nonequivalent. This unperturbed limit for the LR asymmetry relies in the fact that the charge centers are displaced from the triangular lattice sites in the direction perpendicular to the ZZ edge by effect of the kagome sites. Nevertheless, this is not exclusively a feature of the 6B1V model but a general property of MATBG with Wannier orbitals resembling a fidjet spinner [10,27,55].

In addition, as for ZZ edges minivalleys are not coupled and opposite chirality states are placed at different minivalleys; the hybridization between chiral states is also asymmetric inducing anticrossings at different places in the BZ. Panel (f) shows an interplay between the chiral states at  $\bar{P}$  and the trivial ZZ edge state around  $\bar{Q}$  at the left boundary, which hybridizes with the chiral states at the right boundary at  $\bar{Q}$ ; see panel (g).

Finally, in Fig. 9(a) we illustrate the transport properties for a gate voltage potential profile as in Fig. 8 but with a reduced length of the central region to  $\lambda_b \approx 60$  nm in order to obtain a larger overlap between the chiral edge states at the ends of this narrow central region. We observe in this case a small but finite transmission in the gap region which can be associated with the chiral state's hybridization. On the other hand, for the strong coupling case the overlap diminishes because the penetration length decays with  $\delta_S$  and thus the transmission in the gap region becomes negligible; see Fig. 9(b).

## V. CONCLUSIONS AND OUTLOOK

In this work we have analyzed the electronic and transport properties of MATBLG junctions using lattice models. We have considered both the 2B1V model of Ref. [27]

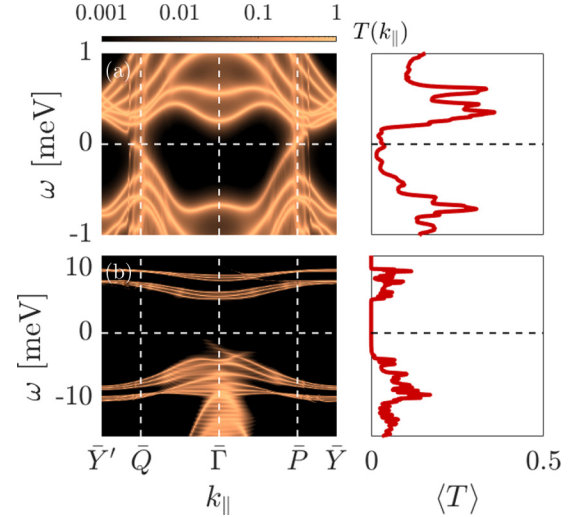


FIG. 9. Two-terminal transport properties for a three region junction N-CNP-N with ZZ orientation. Panel (a): weak coupling limit with the substrate  $\delta_S = 0.1$  meV. Panel (b): strong coupling limit with the substrate  $\delta_S = 10$  meV plus breaking of translational symmetry with  $\delta_{CDW} = 1$  meV. Left column: spectral representation of the transmission at the junction in log scale. Right column: solid red line represents the average transmission of the nearly flat bands. The length of the central region is  $\lambda_b \approx 90$  ( $\lambda_b^{ZZ} = 4L_x$ ) nm and its Fermi energy is kept at the CNP, while the normal regions N are heavily doped with  $E_F = -140$  meV.

and the 6B1V model of Ref. [35], the last one accounting for fragile topology and consequently hosting topological edge states in the presence of symmetry breaking perturbations.

Regarding the transport properties between MATBLG regions doped at the flat bands through a barrier, we have found that these are not sensitive to topology and thus both the 2B1V and the 6B1V models give qualitatively similar results. In contrast, for a three region junction where the central one is fixed at the CNP and the lateral ones are heavily doped, transport and LDOS are determined by the hybridization of chiral states running in opposite directions at the interfaces. As we have shown, an asymmetry in the LDOS between the left and right interface appears which could allow one to distinguish the orientation of the junction with respect to the moiré lattice by means of STM experiments.

As an outlook, we foresee several possible applications of the method developed in the present work. On the one hand, an extension to a Bogoliubov-de Gennes formulation would allow one to study Josephson and Andreev transport in MATBLG junctions including superconducting correlations [56–58], in line with recent experiments [9]. This type of calculation could help to identify the symmetry of the order parameter in superconducting MATBLG, which is at present an open issue attracting great interest [46,59–62]. Similar calculations have been implemented in the past by some of the authors for the case of pristine graphene layers in proximity with unconventional and topological superconductors [63]. Another extension of our work could be oriented to analyze the possible higher-order topological insulating states

in MATBLG and the appearance of corner states associated to the gapped moiré bound states [26,30,52–54].

### ACKNOWLEDGMENTS

We acknowledge fruitful discussions with L. Brey, P. Burset, Ch. de Beule, P. Recher, and T. Stauber and thank all of them for useful comments on this manuscript. This project has been funded by the Spanish MICINN through Grant No. FIS2017-84860-R and by the María de Maeztu Programme for Units of Excellence in Research and Development Grant No. CEX2018-000805-M.

### APPENDIX A: 6B1V HAMILTONIAN WITH UNIT CELL DOUBLING

As defined in the main text, for the 6B1V model we consider a doubled unit cell leading to an orthogonal lattice with vectors  $L_x = \sqrt{3}L_m$  and  $L_y = L_m$  and local fermion operators  $\hat{\Psi} = (\hat{\Psi}_A \ \hat{\Psi}_B)^T$ , with  $\hat{\Psi}_\mu = (\hat{\tau}_{p_z, \mu} \ \hat{\tau}_{p_+, \mu} \ \hat{\tau}_{p_-, \mu} \ \hat{\kappa}_{s, \mu}^{(1)} \ \hat{\kappa}_{s, \mu}^{(2)} \ \hat{\kappa}_{s, \mu}^{(3)})^T$ , where  $\mu \equiv A, B$  indicates the two sites within the doubled unit cell. The 6B1V Hamiltonian in this basis adopts the general form

$$\hat{\mathcal{H}}_{cd}^{(6)}(\mathbf{k}) = \begin{pmatrix} \hat{H}^{AA} & \hat{H}^{AB} \\ \hat{H}^{AB\dagger} & \hat{H}^{AA} \end{pmatrix}, \quad (\text{A1})$$

where

$$\hat{H}^{AA} = \begin{pmatrix} H_{p_z}^{AA} + \mu_{p_z} & \hat{C}_{p_\pm p_\pm}^{AA} & \hat{0} \\ \hat{C}_{p_\pm p_\pm}^{AA\dagger} & \hat{H}_{p_\pm}^{AA} + \mu_{p_\pm} \hat{\mathbb{I}}_2 & \hat{C}_{\kappa p_\pm}^{AA} \\ \hat{0} & \hat{C}_{\kappa p_\pm}^{AA\dagger} & \hat{H}_{\kappa}^{AA} + \mu_{\kappa} \hat{\mathbb{I}}_3 \end{pmatrix}, \quad \hat{H}^{AB} = \begin{pmatrix} H_{p_z}^{AB} & \hat{C}_{p_\pm p_\pm, 1}^{AB} & \hat{0} \\ \hat{C}_{p_\pm p_\pm, 2}^{AB} & \hat{H}_{p_\pm}^{AB} & \hat{C}_{\kappa p_\pm, 1}^{AB} \\ \hat{0} & \hat{C}_{\kappa p_\pm, 2}^{AB} & \hat{H}_{\kappa}^{AB} \end{pmatrix}. \quad (\text{A2})$$

We now define all the contributions to the total Hamiltonian classified for its orbital character. First the nearest-neighbor standard hopping for  $(\tau, p_z)$  orbitals in a cd basis:

$$H_{p_z}^{AA} = t_{p_z}(\phi_{0\bar{1}} + \phi_{01}), \quad H_{p_z}^{AB} = t_{p_z}[1 + \phi_{0\bar{1}}(1 + \phi_{10}) + \phi_{10}], \quad (\text{A3})$$

where  $\phi_{10} = e^{-ik_x L_x}$  and  $\phi_{01} = e^{-ik_y L_y}$  with  $\phi_{ij} = \phi_{ij}^\dagger$ .

For the triangular lattice  $(\tau, p_\pm)$  orbitals we have the following intraorbital terms:

$$\hat{H}_{p_\pm, 0}^{AA} = t_{p_\pm}(\phi_{0\bar{1}} + \phi_{01})\hat{\mathbb{I}}_2, \quad \hat{H}_{p_\pm, 0}^{AB} = t_{p_\pm}[1 + \phi_{0\bar{1}}(1 + \phi_{10}) + \phi_{10}]\hat{\mathbb{I}}_2, \quad (\text{A4})$$

and the interorbital terms

$$\begin{aligned} \hat{C}_{p_\pm p_\pm}^{AA} &= \begin{pmatrix} 0 & t_{p_\pm p_\pm}^+ \phi_{0\bar{1}} + t_{p_\pm p_\pm}^- \phi_{01} \\ t_{p_\pm p_\pm}^+ \phi_{01} + t_{p_\pm p_\pm}^- \phi_{0\bar{1}} & 0 \end{pmatrix}, \\ \hat{C}_{p_\pm p_\pm}^{AB} &= \begin{pmatrix} 0 & t_{p_\pm p_\pm}^+(w + w' \phi_{10}) + t_{p_\pm p_\pm}^-(w' \phi_{0\bar{1}} + w \phi_{01} \phi_{10}) \\ t_{p_\pm p_\pm}^+(w' \phi_{0\bar{1}} \phi_{10} + w \phi_{0\bar{1}}) + t_{p_\pm p_\pm}^-(w' + w \phi_{10}) & 0 \end{pmatrix}, \end{aligned} \quad (\text{A5})$$

where  $w = e^{i2\pi/3}$  and  $w'$  is the complex conjugate of  $w$ . This phase accounts for the different orientation of  $(\tau, p_\pm)$  orbitals. We can change valley with the transformation  $w \rightarrow w'$ . The final expression of the total Hamiltonian for this subspace has the form

$$\hat{H}_{p_\pm}^{AA} = \hat{H}_{p_\pm, 0}^{AA} + \hat{C}_{p_\pm p_\pm}^{AA}, \quad \hat{H}_{p_\pm}^{AB} = \hat{H}_{p_\pm, 0}^{AB} + \hat{C}_{p_\pm p_\pm}^{AB}, \quad (\text{A6})$$

which contains the fundamental symmetries that protect the Dirac nodes in the triangular lattice. Next we consider the hopping terms concerning the kagome lattice  $(\kappa, s)$  orbitals, which include first and second nearest neighbor contributions within this subspace in the form

$$\begin{aligned} \hat{H}_{\kappa}^{AA} &= t_{\kappa} \begin{pmatrix} 0 & 1 & 1 \\ 1 & 0 & 1 + \phi_{0\bar{1}} \\ 1 & 1 + \phi_{01} & 0 \end{pmatrix} + t'_{\kappa} \begin{pmatrix} 0 & \phi_{01} & \phi_{0\bar{1}} \\ \phi_{0\bar{1}} & 0 & 0 \\ \phi_{01} & 0 & 0 \end{pmatrix}, \\ \hat{H}_{\kappa}^{AB} &= t_{\kappa} \begin{pmatrix} 0 & 1 & \phi_{0\bar{1}} \\ \phi_{0\bar{1}} \phi_{10} & 0 & 0 \\ \phi_{10} & 0 & 0 \end{pmatrix} + t'_{\kappa} \begin{pmatrix} 0 & \phi_{0\bar{1}} & 1 \\ \phi_{10} & 0 & \phi_{0\bar{1}}(1 + \phi_{10}) \\ \phi_{10} \phi_{0\bar{1}} & 1 + \phi_{10} & 0 \end{pmatrix}. \end{aligned} \quad (\text{A7})$$

On the other hand, the coupling terms between the  $(\tau, p_z)$  and the  $(\tau, p_\pm)$  orbitals are given by

$$\begin{aligned} \hat{C}_{p_\pm p_z}^{AA} &= i \begin{pmatrix} -t_{p_\pm p_z}^+ \phi_{0\bar{1}} + t_{p_\pm p_z}^- \phi_{01} \\ t_{p_\pm p_z}^+ \phi_{01} - t_{p_\pm p_z}^- \phi_{0\bar{1}} \end{pmatrix}^T, \\ \hat{C}_{p_\pm p_z, 1}^{AB} &= i \begin{pmatrix} -t_{p_\pm p_z}^+(w + w' \phi_{10}) + t_{p_\pm p_z}^-(w' \phi_{0\bar{1}} + w \phi_{0\bar{1}} \phi_{10}) \\ t_{p_\pm p_z}^+(w \phi_{0\bar{1}} + w' \phi_{0\bar{1}} \phi_{10}) - t_{p_\pm p_z}^-(w' + w \phi_{10}) \end{pmatrix}^T, \\ \hat{C}_{p_\pm p_z, 2}^{AB} &= i \begin{pmatrix} t_{p_\pm p_z}^+(w \phi_{0\bar{1}} + w' \phi_{0\bar{1}} \phi_{10}) - t_{p_\pm p_z}^-(w' + w \phi_{10}) \\ -t_{p_\pm p_z}^+(w + w' \phi_{10}) + t_{p_\pm p_z}^-(w' \phi_{0\bar{1}} + w \phi_{0\bar{1}} \phi_{10}) \end{pmatrix}, \end{aligned} \quad (\text{A8})$$



and finally the coupling orbital terms in the  $(\tau, p_{\pm}) \times (\kappa, s)$  subspaces:

$$\begin{aligned}\hat{C}_{\kappa p_{\pm}}^{AA} &= \begin{pmatrix} 0 & -t_{\kappa p_{\pm}}^{-} w & t_{\kappa p_{\pm}}^{+} w' \\ 0 & t_{\kappa p_{\pm}}^{+} w' & -t_{\kappa p_{\pm}}^{-} w \end{pmatrix}, \\ \hat{C}_{\kappa p_{\pm},1}^{AB} &= \begin{pmatrix} t_{\kappa p_{\pm}}^{+} \phi_{0\bar{1}} \phi_{10} - t_{\kappa p_{\pm}}^{-} \phi_{10} & t_{\kappa p_{\pm}}^{+} w \phi_{10} & -t_{\kappa p_{\pm}}^{-} w' \phi_{0\bar{1}} \phi_{10} \\ t_{\kappa p_{\pm}}^{+} \phi_{10} - t_{\kappa p_{\pm}}^{-} \phi_{0\bar{1}} \phi_{10} & -t_{\kappa p_{\pm}}^{-} w' \phi_{10} & t_{\kappa p_{\pm}}^{+} w \phi_{0\bar{1}} \phi_{10} \end{pmatrix}, \\ \hat{C}_{\kappa p_{\pm},2}^{AB} &= \begin{pmatrix} t_{\kappa p_{\pm}}^{+} - t_{\kappa p_{\pm}}^{-} \phi_{0\bar{1}} & t_{\kappa p_{\pm}}^{+} \phi_{0\bar{1}} - t_{\kappa p_{\pm}}^{-} \\ t_{\kappa p_{\pm}}^{+} w' \phi_{0\bar{1}} & -t_{\kappa p_{\pm}}^{-} w \phi_{0\bar{1}} \\ -t_{\kappa p_{\pm}}^{-} w & t_{\kappa p_{\pm}}^{+} w' \end{pmatrix}. \end{aligned} \quad (\text{A9})$$

The list of the parameters used are given in Table II.

## APPENDIX B: BOUNDARY GREEN'S FUNCTION AND DYSON EQUATIONS

In order to compute the bGF of the  $N \times N$  Hamiltonian in reciprocal space  $\hat{H}(\mathbf{k})$  we decompose the momenta into parallel and perpendicular components  $\mathbf{k} = (k_{\parallel}, k_{\perp})$  relative to the boundary direction that we consider. The bulk Hamiltonian periodicity in both directions is set by  $(L_{\parallel}, L_{\perp})$ , such that  $\hat{H}(\mathbf{k} + 2\pi\mathbf{u}_{\perp}/L_{\perp}) = \hat{H}(\mathbf{k})$ , where  $\mathbf{u}_{\perp}$  is the unitary vector in the perpendicular direction. Thus, for a model with a triangular lattice like the 6B1V model, we have to double the primitive cell to obtain an orthogonal decomposition of the momentum. Using this periodicity, the Hamiltonian can be expanded in a Fourier series,  $\hat{H}(\mathbf{k}) = \sum_n \hat{V}_n(k_{\parallel}) e^{in\mathbf{k}_{\perp} L_{\perp}}$ , where  $n$  is the number of neighbors and Hermiticity implies  $\hat{V}_{-n} = \hat{V}_n^{\dagger}$ .

The advanced bulk GF is then defined as

$$\hat{G}^A(\mathbf{k}, \omega) = [(\omega - i0^{+})\hat{1} - \hat{H}(\mathbf{k})]^{-1}, \quad (\text{B1})$$

where the  $N \times N$  matrix structure is indicated by the hat notation. Fourier transforming along the perpendicular direction, the GF components are given by

$$\hat{G}_{jj'}^A(k_{\parallel}, \omega) = \frac{L_{\perp}}{2\pi} \int_{-\pi/L_{\perp}}^{\pi/L_{\perp}} dk_{\perp} e^{i(j-j')k_{\perp} L_{\perp}} \hat{G}^A(k_{\parallel}, k_{\perp}, \omega), \quad (\text{B2})$$

TABLE II. 6B1V model parameters written in units of the dominant energy scale  $t_{\kappa} = 27$  meV.

Parameter	Meaning	Ratio to $t_{\kappa}$
$t_{p_z}$	$(\tau, p_z)$ NN hopping	0.17
$t_{p_{\pm}}$	$(\tau, p_{\pm})$ NN intraorbital hopping	-0.03
$t_{p_{\pm}p_{\pm}}^{+}$	$(\tau, p_{\pm})$ NN interorbital hopping	-0.065
$t_{p_{\pm}p_{\pm}}^{-}$	$(\tau, p_{\pm})$ NN interorbital hopping	-0.055
$t_{\kappa}$	$(\kappa, s)$ NN hopping	1
$t'_{\kappa}$	$(\kappa, s)$ NNN hopping	0.25
$t_{p_{\pm}p_z}^{+}$	$(\tau, p_{\pm}) \times (\tau, p_z)$ NN hopping	0.095
$t_{p_{\pm}p_z}^{-}$	$(\tau, p_{\pm}) \times (\tau, p_z)$ NN hopping	0.085
$t_{\kappa p_{\pm}}^{+}$	$(\kappa, s) \times (\tau, p_{\pm})$ NN hopping	0.6
$t_{\kappa p_{\pm}}^{-}$	$(\kappa, s) \times (\tau, p_{\pm})$ NN hopping	0.2
$\delta_{p_z}$	$(\tau, p_z)$ chemical potential	-0.2593
$\delta_{p_{\pm}}$	$(\tau, p_{\pm})$ chemical potential	-0.3628
$\delta_{\kappa}$	$(\kappa, s)$ chemical potential	0.20

where  $j$  and  $j'$  are lattice site indices. Following Ref. [38] with the identification  $z = e^{ik_{\perp} L_{\perp}}$ , the integral is converted into a complex contour integral,

$$\hat{G}_{jj'}^A(k_{\parallel}, \omega) = \frac{1}{2\pi i} \oint_{|z|=1} \frac{dz}{z} z^{j-j'} \hat{G}^A(k_{\parallel}, z, \omega). \quad (\text{B3})$$

Finally the integral can be computed taking advantage of the residue theorem from the roots of the characteristic polynomial from  $P(\omega, z) = \det[\omega\hat{1} - \hat{H}(k_{\parallel}, z)]$ . In [43] we describe an efficient method, based on the Fadeev-LeVerrier algorithm, to construct the characteristic polynomial and the adjugate matrix which are needed to evaluate the GF components.

To simplify notation, we omit the superscript “A” in advanced GFs from now on. Given the real-space components of the bulk GF in Eq. (B3), we next extend the method of Refs. [56,64,65] to derive the bGF characterizing a *semi-infinite* 2D dimensional system. To that effect, we add an impurity potential line  $\epsilon$  localized at the frontier region [66]. Taking the limit  $\epsilon \rightarrow \infty$ , the infinite system is cut into disconnected semi-infinite subsystems with  $j \leq -1$  (left side, L) and  $j \geq 1$  (right side, R). Using the Dyson equation [65], the local GF components of the cut subsystem follow as

$$\hat{G}_{jj} = \hat{G}_{jj}^{(0)} - \hat{G}_{j0}^{(0)} [\hat{G}_{00}^{(0)}]^{-1} \hat{G}_{0j}^{(0)}, \quad (\text{B4})$$

where  $\hat{G}^{(0)}$  are the bulk GF and  $\hat{G}$  are the semi-infinite GF. The bGF for the left and right semi-infinite system, respectively, are with Eq. (B4) given by

$$\hat{G}_L(k_{\parallel}, \omega) = \hat{G}_{\bar{1}\bar{1}}(k_{\parallel}, \omega), \quad \hat{G}_R(k_{\parallel}, \omega) = \hat{G}_{11}(k_{\parallel}, \omega). \quad (\text{B5})$$

Using this boundary Green's function we can compute the spectral properties of open systems but also the spectral and transport properties for different types of junctions defined on MATBLG:

$$\hat{G}_{nn} = \hat{G}_{nn} + \hat{G}_n \hat{\Sigma}_{LR}^{\dagger} [\hat{1} - \hat{G}_L \hat{\Sigma}_{LR} \hat{G}_R \hat{\Sigma}_{LR}^{\dagger}]^{-1} \hat{G}_L \hat{\Sigma}_{LR} \hat{G}_{1n}, \quad (\text{B6})$$

where  $\hat{\Sigma}_{LR}^{\dagger}$  is the coupling term between the different regions that define the wall and requires the nonlocal GF for the right semi-infinite system given by

$$\begin{aligned}\hat{G}_{n1} &= \hat{G}_{n1}^{(0)} - \hat{G}_R \hat{T}^{\dagger} \hat{G}_{n1}^{(0)} [\hat{G}_{00}^{(0)}]^{-1} \hat{G}_{01}^{(0)}, \\ \hat{G}_{1n} &= \hat{G}_{1n}^{(0)} - \hat{G}_{10}^{(0)} [\hat{G}_{00}^{(0)}]^{-1} \hat{G}_{1n}^{(0)} \hat{T} \hat{G}_R, \end{aligned} \quad (\text{B7})$$

where  $\hat{T}$  is the coupling term between consecutive sites of each semi-infinite system and

$$\begin{aligned}\hat{G}_{1n}^{(0)} &= \hat{G}_{00}^{(0)}(\hat{T}\hat{G}_R)^{n-1}, \\ \hat{G}_{n1}^{(0)} &= (\hat{G}_R\hat{T}^\dagger)^{n-1}\hat{G}_{00}^{(0)}.\end{aligned}\quad (\text{B8})$$

For computing transport properties in junctions we start from the general expression for the current between two leads using Keldysh Green's functions in [65,67], which we adapt to the one valley MATBLG case

$$\begin{aligned}I_{LR}(k_\parallel) &= \frac{2e}{h} \int d\omega \text{tr}\{\hat{\Sigma}_{LR}\hat{G}_{RR}^{+-}\hat{\Sigma}_{RL}\hat{G}_L^{+-} \\ &\quad - \hat{\Sigma}_{LR}\hat{G}_{RR}^{+-}\hat{\Sigma}_{RL}\hat{G}_L^{+-}\},\end{aligned}\quad (\text{B9})$$

where the factor 2 comes from the spin degree of freedom. Finally we expand the nonequilibrium correlation functions in terms of advanced GF as using Langreth rules

$$\begin{aligned}\hat{G}_{RR}^{+-/-+} &= (\hat{\mathbb{I}} + \hat{G}_{LR}^\dagger \hat{\Sigma}_{LR})\hat{G}_R^{+-/-+}(\hat{\mathbb{I}} + \hat{\Sigma}_{LR}^\dagger \hat{G}_{LR}) \\ &\quad + \hat{G}_{RR}^\dagger \hat{\Sigma}_{LR}^\dagger \hat{G}_L^{+-/-+} \hat{\Sigma}_{LR} \hat{G}_{RR},\end{aligned}\quad (\text{B10})$$

with

$$\begin{aligned}\hat{G}_j^{+-} &= f_j(\omega - \mu_j)(\hat{G}_j - \hat{G}_j^\dagger), \\ \hat{G}_j^{+-} &= [f_j(\omega - \mu_j) - 1](\hat{G}_j - \hat{G}_j^\dagger),\end{aligned}\quad (\text{B11})$$

$j = L/R$  and  $f_j(\omega - \mu_j)$  is the Fermi-Dirac distribution. Using the Dyson equation we can obtain the current in terms of the bGF

$$\begin{aligned}\hat{G}_{LR} &= \hat{G}_L \hat{\Sigma}_{LR} \hat{G}_{RR}, \\ \hat{G}_{RR} &= [\hat{\mathbb{I}} - \hat{G}_R \hat{\Sigma}_{LR}^\dagger \hat{G}_L \hat{\Sigma}_{LR}]^{-1} \hat{G}_R.\end{aligned}\quad (\text{B12})$$

After some algebra we get the Landauer formula

$$I_{LR}(k_\parallel) = \frac{2e}{h} \int d\omega T(k_\parallel, \omega)(f_R - f_L), \quad (\text{B13})$$

where

$$\begin{aligned}T(k_\parallel, \omega) &= \text{tr}\{(\hat{\mathbb{I}} + \hat{G}_{LR}^\dagger \hat{\Sigma}_{LR})(\hat{G}_R - \hat{G}_R^\dagger)(\hat{\mathbb{I}} + \hat{\Sigma}_{LR}^\dagger \hat{G}_{LR}) \\ &\quad \times \hat{\Sigma}_{LR}^\dagger (\hat{G}_L - \hat{G}_L^\dagger)\},\end{aligned}\quad (\text{B14})$$

where  $T(k_\parallel, \omega)$  defines a momentum resolved transmission coefficient and  $\langle T(\omega) \rangle = \frac{1}{n_k} \sum_{k_\parallel} T(k_\parallel, \omega)$  is the normalized total transmission function, which can be associated with a two-terminal zero temperature conductance through  $G = G_0 \langle T(0) \rangle$ , where  $G_0 = 2e^2/h$  is the conductance quantum.

### APPENDIX C: RECURSIVE GF METHOD

In cases where a nonuniform potential is applied the bGF can be calculated recursively. We define the recursive bGF at a dimensionless  $n$  site as

$$[\hat{G}_{L/R}^{rc}(n)]^{-1} = \omega \hat{\mathbb{I}} - \hat{\mathcal{H}}_0(k_\parallel) - \hat{\mathcal{H}}_b(n) - \Sigma_{L/R}(n), \quad (\text{C1})$$

where  $\hat{\mathcal{H}}_0(k_\parallel)$  is the local contribution defined in a stripe and the recursive expression of the self energy takes

the form

$$\begin{aligned}\Sigma_R(n) &= \hat{T}_{LR}[\hat{G}_R^{rc}(n-1)]^{-1}\hat{T}_{LR}^\dagger, \\ \Sigma_L(n) &= \hat{T}_{LR}^\dagger[\hat{G}_L^{rc}(n-1)]^{-1}\hat{T}_{LR}.\end{aligned}\quad (\text{C2})$$

As we can see the self-energy couples the  $n$  site with the previous one and  $n$  goes from  $n = 1$  to  $n = N_x = L/2L_m$ , where  $L$  is the total length of the system. The self energy at the first site  $\Sigma_{L/R}(1)$  can be defined to simulate the coupling to a doped normal lead with constant LDOS inducing a characteristic broadening of the states through the junction.

Inspired by the experimental device described in Ref. [44] the potential profile Hamiltonian for a three regions junction takes the form

$$\begin{aligned}\hat{\mathcal{H}}_b(n) &= \frac{U_b}{2} V_x(n) \hat{\mathbb{I}}, \\ V_x(n) &= \tanh\left(\frac{n - (N_x - N_b) - 1}{d_b}\right) + 1.\end{aligned}\quad (\text{C3})$$

For the 6B1V model and following the polynomial expansion in  $z = e^{ik_\perp L_\perp}$  of the Hamiltonian  $\hat{\mathcal{H}}(z)$  as described in [43] taking the form

$$\begin{aligned}\hat{\mathcal{H}}(z) &= \sum_{i=1}^{2m+1} \hat{H}_i z^{i-(m+1)} \\ &= \hat{H}_1 z^{-m} + \dots + \hat{H}_{m+1} + \dots + \hat{H}_{2m+1} z^m,\end{aligned}\quad (\text{C4})$$

we can define the matrix that defines the recursive method as  $\hat{\mathcal{H}}_0 = \hat{H}_2$ ,  $\hat{T}_{LR} = \hat{H}_1^\dagger$ . We note that this expression is totally general and can be used for any TB nearest neighbor Hamiltonian.

In the case of the 2B1V model, which goes beyond the nearest neighbors approximation, we follow Ref. [44] to set the recursive equations from

$$\begin{aligned}\hat{\mathcal{H}}_0 &= \begin{pmatrix} \hat{H}_0 & \hat{H}_1 & \hat{H}_2 \\ \hat{H}_1^\dagger & \hat{H}_0 & \hat{H}_1 \\ \hat{H}_2^\dagger & \hat{H}_1^\dagger & \hat{H}_0 \end{pmatrix}, \\ \hat{T}_{LR} &= \begin{pmatrix} \hat{H}_3^\dagger & \hat{H}_2^\dagger & \hat{H}_1^\dagger \\ \hat{0} & \hat{H}_3^\dagger & \hat{H}_2^\dagger \\ \hat{0} & \hat{0} & \hat{H}_3^\dagger \end{pmatrix},\end{aligned}\quad (\text{C5})$$

where

$$\begin{aligned}\hat{H}_0 &= \begin{pmatrix} 2t'_2 \sin k_x L_x & t_1 e^{i\frac{k_x L_x}{2}} + t_4^* e^{-i\frac{k_x L_x}{2}} \\ t_1 e^{-i\frac{k_x L_x}{2}} + t_4 e^{i\frac{k_x L_x}{2}} & 2t'_2 \sin k_x L_x \end{pmatrix}, \\ \hat{H}_1 &= \begin{pmatrix} 0 & t_1 + t_5^* e^{ik_x L_x} \\ t_1 + t_5 e^{-ik_x L_x} & 0 \end{pmatrix}, \\ \hat{H}_2 &= \begin{pmatrix} 0 & t_4^* e^{i\frac{k_x L_x}{2}} + t_5^* e^{-i\frac{k_x L_x}{2}} \\ t_4 e^{-i\frac{k_x L_x}{2}} + t_5 e^{i\frac{k_x L_x}{2}} & 0 \end{pmatrix}, \\ \hat{H}_3 &= \begin{pmatrix} -2t'_2 \sin \frac{k_x L_x}{2} & t_5^* \\ t_5 & -2t'_2 \sin \frac{k_x L_x}{2} \end{pmatrix}.\end{aligned}\quad (\text{C6})$$

- [1] S. Carr, D. Massatt, S. Fang, P. Cazeaux, M. Luskin, and E. Kaxiras, *Phys. Rev. B* **95**, 075420 (2017).
- [2] R. Ribeiro-Palau, C. Zhang, K. Watanabe, T. Taniguchi, J. Hone, and C. R. Dean, *Science* **361**, 690 (2018).
- [3] Y. Cao, V. Fatemi, S. Fang, K. Watanabe, T. Taniguchi, E. Kaxiras, and P. Jarillo-Herrero, *Nature (London)* **556**, 43 (2018).
- [4] Y. Cao, V. Fatemi, A. Demir, S. Fang, S. L. Tomarken, J. Y. Luo, J. D. Sanchez-Yamagishi, K. Watanabe, T. Taniguchi, E. Kaxiras *et al.*, *Nature (London)* **556**, 80 (2018).
- [5] C. Ma, Q. Wang, S. Mills, X. Chen, B. Deng, S. Yuan, C. Li, K. Watanabe, T. Taniguchi, X. Du *et al.*, *Nano Lett.* **20**, 6076 (2020).
- [6] M. Serlin, C. Tschirhart, H. Polshyn, Y. Zhang, J. Zhu, K. Watanabe, T. Taniguchi, L. Balents, and A. Young, *Science* **367**, 900 (2020).
- [7] S. Wu, Z. Zhang, K. Watanabe, T. Taniguchi, and E. Y. Andrei, *Nat. Mater.* **20**, 488 (2021).
- [8] P. Stepanov, M. Xie, T. Taniguchi, K. Watanabe, X. Lu, A. H. MacDonald, B. A. Bernevig, and D. K. Efetov, *arXiv:2012.15126*.
- [9] D. Rodan-Legrain, Y. Cao, J. M. Park, S. C. de la Barrera, M. T. Randeria, K. Watanabe, T. Taniguchi, and P. Jarillo-Herrero, *Nat. Nanotechnol.* **16**, 769 (2021).
- [10] F. Guinea and N. R. Walet, *Proc. Natl. Acad. Sci. USA* **115**, 13174 (2018).
- [11] T. Cea, P. A. Pantaleón, and F. Guinea, *Phys. Rev. B* **102**, 155136 (2020).
- [12] J. Liu and X. Dai, *Phys. Rev. B* **103**, 035427 (2021).
- [13] P. Wilhelm, T. C. Lang, and A. M. Läuchli, *Phys. Rev. B* **103**, 125406 (2021).
- [14] N. Bultinck, S. Chatterjee, and M. P. Zaletel, *Phys. Rev. Lett.* **124**, 166601 (2020).
- [15] K. P. Nuckolls, M. Oh, D. Wong, B. Lian, K. Watanabe, T. Taniguchi, B. A. Bernevig, and A. Yazdani, *Nature* **582**, 198 (2020).
- [16] T. Stauber, T. Low, and G. Gómez-Santos, *Phys. Rev. B* **98**, 195414 (2018).
- [17] J. Kang and O. Vafek, *Phys. Rev. Lett.* **122**, 246401 (2019).
- [18] M. Zhang, Y. Zhang, C. Lu, W.-Q. Chen, and F. Yang, *Chin. Phys. B* **29**, 127102 (2020).
- [19] S. Carr, S. Fang, H. C. Po, A. Vishwanath, and E. Kaxiras, *Phys. Rev. Research* **1**, 033072 (2019).
- [20] R. Bistritzer and A. H. MacDonald, *Proc. Natl. Acad. Sci. USA* **108**, 12233 (2011).
- [21] D. Thouless, *J. Phys. C* **17**, L325 (1984).
- [22] A. A. Soluyanov and D. Vanderbilt, *Phys. Rev. B* **83**, 035108 (2011).
- [23] K. Hejazi, C. Liu, H. Shapourian, X. Chen, and L. Balents, *Phys. Rev. B* **99**, 035111 (2019).
- [24] L. Zou, H. C. Po, A. Vishwanath, and T. Senthil, *Phys. Rev. B* **98**, 085435 (2018).
- [25] H. C. Po, H. Watanabe, and A. Vishwanath, *Phys. Rev. Lett.* **121**, 126402 (2018).
- [26] J. Ahn, S. Park, and B.-J. Yang, *Phys. Rev. X* **9**, 021013 (2019).
- [27] M. Koshino, N. F. Q. Yuan, T. Koretsune, M. Ochi, K. Kuroki, and L. Fu, *Phys. Rev. X* **8**, 031087 (2018).
- [28] H.-X. Wang, G.-Y. Guo, and J.-H. Jiang, *New J. Phys.* **21**, 093029 (2019).
- [29] B. A. Bernevig, Z. Song, N. Regnault, and B. Lian, *Phys. Rev. B* **103**, 205411 (2021).
- [30] B. J. Wieder and B. A. Bernevig, *arXiv:1810.02373*.
- [31] M. B. de Paz, M. G. Vergniory, D. Bercioux, A. García-Etxarri, and B. Bradlyn, *Phys. Rev. Research* **1**, 032005(R) (2019).
- [32] S. H. Kooi, G. van Miert, and C. Ortix, *Phys. Rev. B* **100**, 115160 (2019).
- [33] Z. Li, H.-C. Chan, and Y. Xiang, *Phys. Rev. B* **102**, 245149 (2020).
- [34] V. Peri, Z.-D. Song, M. Serra-Garcia, P. Engeler, R. Queiroz, X. Huang, W. Deng, Z. Liu, B. A. Bernevig, and S. D. Huber, *Science* **367**, 797 (2020).
- [35] H. C. Po, L. Zou, T. Senthil, and A. Vishwanath, *Phys. Rev. B* **99**, 195455 (2019).
- [36] K. Hejazi, X. Chen, and L. Balents, *Phys. Rev. Research* **3**, 013242 (2021).
- [37] J. Cao, M. Wang, C.-C. Liu, and Y. Yao, *arXiv:2012.02575*.
- [38] M. Alvarado, A. Iks, A. Zazunov, R. Egger, and A. L. Yeyati, *Phys. Rev. B* **101**, 094511 (2020).
- [39] A. T. Pierce, Y. Xie, J. M. Park, E. Khalaf, S. H. Lee, Y. Cao, D. E. Parker, P. R. Forrester, S. Chen, K. Watanabe *et al.*, *arXiv:2101.04123*.
- [40] Y. Choi, H. Kim, C. Lewandowski, Y. Peng, A. Thomson, R. Polski, Y. Zhang, K. Watanabe, T. Taniguchi, J. Alicea *et al.*, *arXiv:2102.02209*.
- [41] U. Zondiner, A. Rozen, D. Rodan-Legrain, Y. Cao, R. Queiroz, T. Taniguchi, K. Watanabe, Y. Oreg, F. von Oppen, A. Stern *et al.*, *Nature (London)* **582**, 203 (2020).
- [42] S. Kezilebieke, M. N. Huda, V. Vaño, M. Aapro, S. C. Ganguli, O. J. Silveira, S. Głodzik, A. S. Foster, T. Ojanen, and P. Liljeroth, *Nature (London)* **588**, 424 (2020).
- [43] M. Alvarado and A. L. Yeyati, *arXiv:2107.10195*.
- [44] C. De Beule, P. G. Silvestrov, M.-H. Liu, P. Recher *et al.*, *Phys. Rev. Research* **2**, 043151 (2020).
- [45] M. Fujimoto and M. Koshino, *Phys. Rev. B* **103**, 155410 (2021).
- [46] X. Wu, W. Hanke, M. Fink, M. Klett, and R. Thomale, *Phys. Rev. B* **101**, 134517 (2020).
- [47] D. V. Chichinadze, L. Classen, and A. V. Chubukov, *Phys. Rev. B* **102**, 125120 (2020).
- [48] A. Alexandradinata, X. Dai, and B. A. Bernevig, *Phys. Rev. B* **89**, 155114 (2014).
- [49] A. Alexandradinata, Z. Wang, and B. A. Bernevig, *Phys. Rev. X* **6**, 021008 (2016).
- [50] J. Ahn, D. Kim, Y. Kim, and B.-J. Yang, *Phys. Rev. Lett.* **121**, 106403 (2018).
- [51] B. Bradlyn, Z. Wang, J. Cano, and B. A. Bernevig, *Phys. Rev. B* **99**, 045140 (2019).
- [52] M. J. Park, Y. Kim, G. Y. Cho, and S. B. Lee, *Phys. Rev. Lett.* **123**, 216803 (2019).
- [53] M. J. Park, S. Jeon, S. Lee, H. C. Park, and Y. Kim, *Carbon* **174**, 260 (2021).
- [54] B. Liu, L. Xian, H. Mu, G. Zhao, Z. Liu, A. Rubio, and Z. F. Wang, *Phys. Rev. Lett.* **126**, 066401 (2021).
- [55] H. C. Po, L. Zou, A. Vishwanath, and T. Senthil, *Phys. Rev. X* **8**, 031089 (2018).
- [56] P. Burset, A. Levy Yeyati, and A. Martín-Rodero, *Phys. Rev. B* **77**, 205425 (2008).
- [57] P. Burset, W. Herrera, and A. Levy Yeyati, *Phys. Rev. B* **80**, 041402(R) (2009).

- [58] W. J. Herrera, P. Buset, and A. L. Yeyati, *J. Phys.: Condens. Matter* **22**, 275304 (2010).
- [59] H. Guo, X. Zhu, S. Feng, and R. T. Scalettar, *Phys. Rev. B* **97**, 235453 (2018).
- [60] S. Ray, J. Jung, and T. Das, *Phys. Rev. B* **99**, 134515 (2019).
- [61] M. Christos, S. Sachdev, and M. S. Scheurer, *Proc. Natl. Acad. Sci. USA* **117**, 29543 (2020).
- [62] V. Peri, Z.-D. Song, B. A. Bernevig, and S. D. Huber, *Phys. Rev. Lett.* **126**, 027002 (2021).
- [63] O. E. Casas, S. Gomez Páez, A. Levy Yeyati, P. Buset, and W. J. Herrera, *Phys. Rev. B* **99**, 144502 (2019).
- [64] L. Arrachea, G. S. Lozano, and A. A. Aligia, *Phys. Rev. B* **80**, 014425 (2009).
- [65] A. Zazunov, R. Egger, and A. Levy Yeyati, *Phys. Rev. B* **94**, 014502 (2016).
- [66] S. Pinon, V. Kaladzhyan, and C. Bena, *Phys. Rev. B* **101**, 115405 (2020).
- [67] J. C. Cuevas, A. Martín-Rodero, and A. Levy Yeyati, *Phys. Rev. B* **54**, 7366 (1996).